BNL-229378-2026-JAAM

Rational design of high-performance low-loading oxygen reduction catalysts for alkaline fuel cells

H. Li, E. Stavitski

To be published in "Nature Materials"

February 2026

Photon Sciences

Brookhaven National Laboratory

U.S. Department of Energy

USDOE Office of Science (SC), Basic Energy Sciences (BES). Scientific User Facilities (SUF)

DISCLAIMER

Rational Design of High-Performance Ultra-Low Loading Oxygen Reduction Catalysts for Alkaline Fuel Cells

Huiqi Li[†1], Rui Zeng[†1], Zixiao Shi[1], Hongsen Wang[1], Denis Leshchev[2], Eli Stavitski[2], Miriam M. Tellez-Cruz[1], Weixuan Xu[1], Mi-Ju Kim[1], Andrés Molina Villarino[1], Qihao Li[1], David A. Muller[3,4]*, Héctor D. Abruña[1]*

[1]Department of Chemistry and Chemical Biology, Cornell University, Ithaca, NY 14853, USA.

[2]National Synchrotron Light Source II, Brookhaven National Laboratory, Upton, NY 11973, USA.

[3]School of Applied and Engineering Physics, Cornell University, Ithaca, NY 14853, USA.

[4]Kavli Institute at Cornell for Nanoscale Science, Cornell University, Ithaca, NY 14853, USA.

[†]These authors contributed equally to this work.

*Corresponding author: david.a.muller@cornell.edu; hda1@cornell.edu

ABSTRACT

The lack of mechanistic understanding and catalyst design principles in alkaline electrolytes, especially on the sluggish oxygen reduction reaction (ORR), has impeded the advancement of alkaline fuel cells. Here we developed a modified volcano plot and applied this rationale to strategically design Pt nanosheets with PdH_x nanosheets substrate (PdH_x@Pt NS). This catalyst exhibited remarkable stability with a specific activity of 1.42 mA cm^{-2} at 0.95 V vs. reversible hydrogen electrode (RHE), surpassing benchmark Pt/C by 43 times. Comprehensive characterizations revealed that such impressive performance originated from expansively strained Pt {111} facets, improved oxidative stability and supressed carbon corrosion. Employed as a cathode electrode, PdH_x@Pt NS enabled a peak power density (PPD) at 1.67 W cm^{-2} with a loading of 10 $\mu g_{PGM\ Cathode} cm^{-2}$. Further optimization delivered a record-high PPD of 21.7 W $mg^{-1}_{PGM\ Cathode+Anode}$ and record-low total specific catalyst cost US$ 1.27 kW^{-1}, satisfying the US Department of Energy's platinum group metal (PGM) loading and cost targets. This study provides valuable insights into catalyst design for alkaline ORR and marks a milestone in ultra-low loading PGM catalyst systems.

Anion exchange membrane fuel cells (AEMFCs) hold great promise as the next-generation hydrogen fuel cell technology, offering wider catalyst options than proton exchange membrane fuel cells (PEMFCs) due to better stability in alkaline electrolytes[1]. However, the sluggish kinetics of oxygen reduction reaction (ORR) remains one of major roadblocks hindering their widespread deployment. Understanding the reaction mechanism is key to designing high-performance catalysts and thus advancing these technologies. Nevertheless, current understanding of the ORR mechanism is predominantly based on studies conducted in acidic media, leaving a significant knowledge gap for the alkaline ORR.

One commonly used descriptor for the ORR performance in acidic media is the adsorption energy of oxygen or hydroxyl species (*O or *OH)[2,3]. The Sabatier principle suggests an optimal activity with an intermediate adsorption energy[4,5]. Thus, this principle forms the basis of a typical volcano plot correlating ORR activity with binding energy[6,7]. Pt represents the most active single metal electrocatalyst since it is located closer to the top of the plot, relative to other metals. Considering that its binding energy is larger than the optimal value (according to the plot) weakening of the binding strength should boost the ORR activity. This rationale has successfully guided the prediction and design of numerous Pt-based ORR catalysts in acidic media[8,9]. However, the same trend doesn't hold in alkaline media[10]. One typical example is Pd, which exhibits lower activity than Pt in acid due to stronger oxygen binding, yet garners attention in alkaline media for its reported superior ORR activity compared to Pt[11–14]. This discrepancy underscores the significant influence of electrolyte pH on ORR kinetics, necessitating a reassessment of ORR mechanisms for alkaline media and catalyst design strategies[15,16].

In this manuscript, we aim to advance the understanding of the ORR in alkaline media and close the knowledge gap for catalyst design. We have developed/constructed a modified volcano plot positioning Pd near the top in alkaline media by considering the effect(s) of the coverage of OH_{ad} (Θ_{*OH}) and the electric field. Based on this, our predictions suggest that expansive strain in Pt will promote its ORR activity in alkaline conditions. Following this concept, we prepared a sandwich-like core@shell structure, namely, PdH_x@Pt nanosheets (NS). Incorporating Pt nanosheets with {111} facets onto PdH_x NS enabled expansive strain with high specific surface area, while simultaneously addressing the weak oxidation stability of palladium. The as-synthesized catalyst displayed a mass and specific activity of 0.75 A mg^{-1} and 1.42 mA cm^{-2} at 0.95 V vs. RHE, respectively, ~24 and ~43 times higher than those of commercial Pt/C. O*perando* studies, based

on synchrotron-based X-ray absorption spectroscopy (XAS) and differential electrochemical mass spectrometry (DEMS), demonstrate that the lower Θ_{*OH} on the Pt{111} surface in PdH_x@Pt NS and mitigated carbon corrosion also contribute to the enhanced activity and durability in alkaline media. Under realistic fuel cell working conditions, the PdH_x@Pt NS cathode, with an ultra-low loading of 10 μg cm^{-2}, exhibited a remarkable peak power density (PPD) of 1.67 W cm^{-2} at 4.7 A cm^{-2}, outperforming that of commercial Pt/C (0.75 W cm^{-2}). The PPD could be retained at 1.3 W cm^{-2} even after the loading (including cathode and anode) was reduced to 60 μg cm^{-2}, representing a new record in terms of total PGM catalyst loading and specific catalyst cost reported in the literature. Insights from this study can guide the design and synthesis of tailored catalysts with optimal ORR performance and ultra-low catalyst loading in alkaline media, thereby contributing to the advancement of AEMFCs, in particular, and renewable energy technologies, in general.

Results and Discussions

ORR activities of *O-strong binding metals: Comparison between alkaline and acidic media. Evaluated with a rotating disk electrode (RDE) setup, the half-wave potentials ($E_{1/2}$) of the ORR polarization profiles of carbon supported nanocatalysts (Pt/C, Pd/C, Ir/C, Rh/C, and Ru/C) showed notable positive shifts in alkaline electrolytes compared to acidic ones (Figs. 1a-e). This observation indicates the enhanced ORR activity in alkaline electrolytes is a general phenomenon for this series of catalysts. Notably, in alkaline electrolytes, Pd/C exhibited higher activity than Pt/C, representing the most active one among the studied catalysts (Fig. S1). However, this activity trend cannot be explained by the traditional volcano plot, where Pt typically outperforms than Pd[7]. To eliminate the effects of size and facets, polycrystalline electrodes were used to further investigate the activity relationship between Pd and Pt at different pH values (Figs. S2a-e). The polarization curves again showed that the ORR performance of polycrystalline Pd could rival, and even surpass that of polycrystalline Pt at higher pH values, despite polycrystalline Pd being significantly less active than Pt at lower pHs (Fig. S2f). A similar trend was also observed for polycrystalline Ru and Ir (Fig. S3). These observations suggest that the enhanced ORR performance in alkaline media is not exclusive to a specific material but likely reflects a change of the surface chemistry.

Two major factors can be used to explain the enhanced ORR kinetics with increasing pH values. The first pertains to the changes of Θ_{*OH} on the surface of catalysts. Figs. 1g-h present dynamic edge features acquired from *operando* X-ray absorption near edge structure (XANES)

spectra at the Pt L_3-edge and Pd K-edge, recorded under potential scanning from 0.05 V to 1.10 V vs. RHE in O_2 saturated 1.0 M KOH or $HClO_4$ solution (see Methods). The periodic changes of the plotted data points, indicate synchronized shifts in valence or oxidation state of the metal center as a function of the applied potential[17–19]. While the trend of white line intensity in response to the potentials of Pt/C were similar for both acidic and alkaline electrolytes, the amplitude of this change was significantly larger in alkaline electrolyte (Fig. 1g), suggesting a higher Θ_{*OH} on Pt surface in alkaline media[20,21]. Similar reasoning is also applicable toward Pd/C, in which more drastic changes of the i_1/i_2 ratio of Pd were observed in alkaline electrolyte (Fig. 1h and Fig. S4). These two examples unambiguously establish that the Θ_{*OH} increases significantly in base, likely due to a higher concentration of hydroxide ions (OH^-) at high pH values.

The adsorbed OH_{ad} could play two roles in alkaline media. Firstly, it could serve as a spectator species hindering the adsorption of O_2 on active sites, which would, in turn, decrease the ORR activity because a higher Θ_{*OH} should result in a lower pre-exponential factor ($1-\Theta_{*OH}$) in the rate expression[2,22]. Since OH_{ad} tends to preferentially adsorb on low-coordinated sites, such as step sites or concave sites[2,23], Pt (or other noble metals) nanoparticles should have higher Θ_{*OH}, and thus lower ORR activity compared to Pt nanocrystals with selectively exposed {111} facets in alkaline media. Secondly, OH_{ad} could interact with strongly adsorbed $^*O$ species, and a higher coverage in alkaline media may induce stronger repulsive interactions that destabilize the adsorption of $^*O$, leading to enhanced ORR activity. Thus, it is essential to consider Θ_{*OH} when optimizing the availability of active sites and binding energy of $^*O$ species in alkaline media.

The other factor that likely impacts the ORR in alkaline media is the change in interfacial electric field, which could (and likely does) alter the binding energy of the intermediates involved in the ORR reaction and thus affects the overall reaction kinetics[24,25]. For example, the potential of zero charge (E_{pzc}) of Pt (111) shifts by about 59 mV per pH unit under the RHE scale[26], ranging from 0.34 V (vs. RHE) at pH 1 to approximately 1.0 V (vs. RHE) at pH 14. This shift relocates the E_{pzc} within the oxygen reduction region in alkaline media, yielding a neutrally or slightly negatively charged electrode interface with the weakened electric field. In contrast, the negatively shifted E_{pzc} in acidic media results in a positively charged electrode interface with a much stronger interfacial electric field. Consequently, the weakened electric field in alkaline electrolytes could weaken the binding of reaction intermediates, such as $^*OH$[25,27]. From this perspective, the $^*O$-strong binding catalysts should have higher ORR activity in base when compared to acid.

Modified volcano plot for ORR activity in alkaline media. Based on our experimental results, we propose a modified volcano plot to predict the ORR activity of *O-strong binding catalysts in alkaline media (Fig. S5). Changes in electric field and Θ_{*OH} can impact the ORR activity in alkaline media by reducing the *O binding energy compared to acidic conditions. Among the studied metals, Pd exhibits the highest activity in alkaline media since its *O binding energy is shifted closer to the peak of the plot. While Pt also displays improved ORR activity in alkaline media, it "overshoots" the peak and shows lower activity than Pd due to the excessively weakened oxygen binding. Therefore, when the ORR activity is plotted against oxygen-binding energy without considering the effect of electric field or Θ_{*OH}, the observed tendency in alkaline media notably differs from that in acidic electrolytes (Fig. 1f). The modified volcano plot suggests that the introduction of tensile strain in Pt, which upshifts the Pt d-band center relative to the Fermi level, should benefit ORR performance in alkaline media, in contrast to acidic media[28].

Designing highly active ORR catalysts in alkaline media. The modified volcano plot identifies Pd as the most promising ORR catalyst in alkaline media, consistent with the literature on Pd-based catalysts[13,14]. However, the weak oxidative stability of Pd, especially under the oxygen-rich and high-temperature conditions, limits its performance in fuel cells[11,29]. In contrast, Pt displays stronger oxidative stability despite lower ORR activity. Thus, we aim to design active and stable ORR catalysts by leveraging the superior oxidative stability of Pt. Given that Pt {111} represents the most active Pt facet in alkaline ORR[15], the intent would be to design Pt catalysts with predominantly exposed {111} facets, which can be realized by Pt nanosheets. However, synthesizing Pt nanosheets with {111} facets is challenging and, to the best of our knowledge, has not yet been reported[21]. Here, we overcome this challenge by employing PdH_x NS as a substrate for synthesizing Pt nanosheets with exposed {111} facets. Moreover, considering that the lattice parameter of PdH_x is adjustable by varying its hydrogen content[30], it is possible to expansively strain the surface Pt layer to its optimal value. This expansive strain in Pt should be able to render increased oxygen binding strength and thus improve the ORR activity according to the modified volcano plot in alkaline media (Fig. S5 and Fig. 1f).

The target catalyst was synthesized via a solvothermal method (see Methods). Energy dispersive X-ray (EDX) mapping analysis indicates a uniform distribution of Pt on the surface of the PdH_x nanosheets, forming a sandwich-like core@shell structure (PdH_x@Pt NS), with a thickness of ~ 4 nm and a Pt:Pd atomic ratio of 44:56 (Figs. 2a-b and Figs. S6-7). The time

evolution studies of PdH_x@Pt NS formation during synthesis (Fig. S8 and Fig.2c) elucidated the growth mechanism, indicating that Pt grows on the surface of PdH_x NS. Synchrotron-based XAS (Figs. 2d-g) was employed to further characterize the structure of PdH_x@Pt NS. By comparing the Pd K-edge XANES spectra of PdH_x@Pt NS with those of Pd foil, we identified a reduced energy difference between the first and second peaks, indicating the formation of Pd hydride in PdH_x@Pt NS (Fig. 2d) [11,31,32]. Additionally, the Fourier transform (FT) of the extended X-ray absorption fine structure (EXAFS) spectra (Fig. 2e) revealed a larger Pd-Pd/Pt radial distance in the first scattering shell of PdH_x@Pt NS when compared to Pd foil, likely due to the H incorporation. The XANES spectra at the Pt L_3-edge (Fig. 2f) demonstrated that the Pt features in PdH_x@Pt NS resemble those of Pt foil, indicating a predominantly metallic character. Compared to that of Pt foil and commercial Pt/C, the longer Pt-Pt/Pd radial distance for the first coordination shell of PdH_x@Pt NS (Fig. 2g) suggests a lattice expansion in the Pt layer, consistent with the XRD and electron diffraction pattern results (Fig. 2h and Fig. S9). This lattice expansion should, correspondingly, lead to an upshift of the d-band center[33,34]. This analysis was further validated by the surface valence band spectra of X-ray photoelectron spectroscopy (XPS) (Fig. 2i). Thus, the lattice expansion in Pt should benefit the ORR performance of PdH_x@Pt NS based on the modified volcano plot.

Electrocatalytic evaluation and *operando* characterization of catalysts. The electrochemical characterization was first performed using cyclic voltammetry (Fig. 3a) in Ar-saturated 1.0 M KOH electrolyte. In contrast to commercial Pt/C, commercial Pd/C and PdH_x NS, the voltametric profiles of PdH_x@Pt NS showed distinctive features of the hydrogen underpotential deposition (H_{UPD}) region, resembling those of Pt{111} single crystals in alkaline electrolytes[35,36]. This resemblance indicated that the surface of PdH_x@Pt NS is dominated by Pt{111} facets. Furthermore, the dominance of a particular facet is also supported by the narrow oxidation peak of PdH_x@Pt in CO stripping voltammogram (Fig. S10)[37].

The alkaline ORR performance of the catalysts was evaluated in O_2-saturated 1.0 M KOH solution. As shown in the polarization curves (anodic scans, Fig. 3b), PdH_x@Pt NS exhibited the highest half-wave potential ($E_{1/2}$, 0.968 V), followed by PdH_x NS, Pd/C and Pt/C (Table S1). Though the enhancement of the $E_{1/2}$ in the anodic scans of PdH_x@Pt NS was limited, a remarkable improvement of 43 mV was achieved in the cathodic scans (Fig.S11). This significant change unambiguously demonstrated that Pt played a key role in enhancing the oxidative stability of

PdH_x@Pt NS, which may benefit its long-term durability under high temperature conditions[11,29]. When the ORR activity was quantified in terms of the mass activity (MA) and specific activity (SA) at 0.95 V vs. RHE of the anodic scans, PdH_x@Pt NS exhibited an MA and SA of 0.75 A mg^{-1} and 1.42 mA cm^{-2}, respectively, which are ~24 and ~43 times higher than those of Pt/C (Fig. 3c). Conversely (and as would be anticipated), Pt/C displayed the highest ORR activity among the studied catalysts in 0.1 M $HClO_4$ electrolyte (Figs. 3d-f). This activity comparison between Pt/C and PdH_x@Pt NS in acid can be explained using the traditional volcano plot in which the increased oxygen binding energy, due to an expansive strain, is believed to suppress the ORR activity. However, the opposite tendency, observed in alkaline solution, can only be understood using the modified volcano plot.

Operando XAS was employed to further investigate the superior ORR activity and oxidative stability of PdH_x@Pt NS in alkaline media (Fig. 4). Figs. 4a-b present XANES spectra at the Pt L_3-edge of PdH_x@Pt NS and Pt/C in 1.0 M KOH, acquired under steady state conditions from 0.30 V to 1.10 V vs. RHE. Notably, the intensity of the white line at ~11566 eV increased with increasing potentials, due to enhanced charge transfer from Pt to oxygenated species (*OH or *O) accumulated on the Pt surface at higher potentials[20,38]. Compared to Pt/C (Fig. 4b and Fig. S12b), the changes of the white line intensity in PdH_x@Pt NS with respect to the applied potentials were relatively smaller (Fig. 4a and Fig. S12a). This contrast can be further supported by the relative changes in absorption peaks ($(\Delta\mu_E - \Delta\mu_{0.3V})/\Delta\mu_{0.3V}$) in Fig. 4c and Figs. S13-14, in which PdH_x@Pt NS displayed a much higher level of reversibility and stability than Pt/C (Fig. S14).

To further examine the adsorbed species under polarization conditions, we employed the delta mu ($\Delta\mu$) method, a surface-sensitive technique for identifying surface/adsorbate interactions[39,40]. As shown in Figs. 4d-e, prominent peaks at around 11566 eV can be easily identified and their intensities rose as the applied potentials increased. These peaks arose from the adsorption of *OH or *O at atop sites of Pt, followed by n-fold bonded configurations at higher potentials[20]. Comparatively, $\Delta\mu$ spectra of PdH_x@Pt NS displayed significantly smaller changes than those observed for Pt/C, suggesting a lower Θ_{*OH} with the applied potentials. As schematically depicted in Fig. 4f, the surface of PdH_x@Pt NS tends to adsorb fewer *OH or *O species compared to Pt nanoparticles, giving rise to more active sites and thus likely contributing to the observed superior performance. We speculate that such low coverage of surface *OH and/or *O species on PdH_x@Pt NS is likely due to the unique Pt nanosheet structure with exposed {111} facets, which adsorbs

those species more weakly when compared to other facets on Pt nanoparticles[23].

To understand the role of Pt and Pd in PdH_x@Pt NS under operating conditions, we tracked the dynamic changes in the XANES spectra in alkaline electrolytes, similar to the strategy described in Figs. 1g-h. Compared to Pt/C, PdH_x@Pt NS exhibited much weaker changes in the white line of the Pt L_3-edge during potential scans (Fig. 4g), indicating a lower coverage of *OH or *O species, consistent with the characteristics observed under potentiostatic conditions (Figs. 4a-f). Similarly, when evaluating the i_1/i_2 ratio of Pd K-edge between PdH_x NS and Pd/C (Fig. 4h), we observed that PdH_x NS displayed noticeably smaller changes in the peak ratio, corresponding to smaller changes in the oxidation state of Pd. This distinction can be understood by considering the dominance of Pd {111} facets in the PdH_x nanosheet structure, which exhibits weaker OH adsorption than any other facets, in a manner similar to Pt. Additionally, PdH_x@Pt NS showed an overall higher i_1/i_2 value at the Pd K-edge when compared to PdH_x NS (Fig. 4i), indicating the charge transfer from Pd to Pt. This observation is consistent with its corresponding lower oxidation state observed at the Pt L_3-edge in Fig. 4g.

Durability evaluation and fuel cell testing of catalysts. The long-term durability of the catalysts was assessed using an accelerated durability testing (ADT) protocol with potential cycling between 0.6 and 0.95 V for 10,000 cycles. After the ADT testing, PdH_x@Pt NS exhibited an almost negligible change in $E_{1/2}$ (−1 mV) versus Pt/C (−15 mV) (Fig. 5a), and maintained their original morphology (Fig. 5b). XANES and EXAFS spectra of the Pt L_3-edge (Figs. 5c-d and Fig. S15) indicated minor changes in the geometric configuration and electronic structure of PdH_x@Pt NS after the ADT cycles (Fig. 5c and Fig. S15a). In contrast, the observed notable changes of Pt/C were likely due to the increased Pt particle size caused by Ostwald ripening and/or agglomeration of coalescence (Fig. 5d and Fig. S15b)[41]. To further identify if carbon corrosion also contributed to the degradation of the catalysts, DEMS was employed to measure and quantify the electrogenerated CO_2 product[42]. As show in Fig. 5e, the DEMS results clearly identified strong CO_2 signals when Pt/C catalysts were polarized more positively. In contrast, no feature associated with potential-induced CO_2 formation was observed for PdH_x@Pt NS catalysts. This indicates that PdH_x@Pt NS catalysts can suppress the oxidation of carbon compared to Pt/C, which likely contributed to the long-term structural integrity by preventing PdH_x@Pt NS from detachment or agglomerating.

The temperature-dependent studies were conducted to further evaluate the ORR performance

of PdH_x@Pt NS at elevated temperatures up to 80 °C, since the AEMFC testing based on membrane electrode assemblies (MEA) is typically operated between 60 °C and 80 °C. The ORR polarization curves for PdH_x@Pt NS and Pt/C at different temperatures are summarized in Fig. S16. The plot of ORR activity versus temperature exhibited a similar nonmonotonic trend for both PdH_x@Pt NS and Pt/C (Fig. 5f), likely due to a competition between thermal activation and surface oxidation[11]. Unlike prior findings with PdH_x NS[11], PdH_x@Pt NS consistently outperformed Pt/C across the entire temperature range, highlighting the role of Pt layer in enhancing its oxidative stability. These results strongly suggested that PdH_x@Pt NS could deliver superior performance under the harsher fuel cell testing conditions.

A comparative study was conducted to assess the performance of PdH_x@Pt NS or Pt/C as the cathode catalyst under real feal cell testing conditions. Figs. 6a-b show the polarization curves of AEMFCs operated under H_2-O_2 mode with cathode catalyst loadings of 0.1 mg_{metal} cm^{-2} and 0.01 mg_{metal} cm^{-2}, respectively. For a cathode loading of 0.1 mg_{metal} cm^{-2}, PdH_x@Pt NS exhibited a remarkable PPD of 1.87 W cm^{-2} at 4.5 A cm^{-2}, surpassing the value of Pt/C by more than 400 mW cm^{-2} (Fig. 6a). Even at a 10-fold lower cathode loading (0.01 mg_{metal} cm^{-2}), PdH_x@Pt NS retained a PPD of 1.67 W cm^{-2} (Fig. 6b), significantly outperforming that of Pt/C (0.75 W cm^{-2}). This highlights the effectiveness of PdH_x@Pt in reducing the catalyst cost while maintaining a high performance. Moreover, the AEMFC with PdH_x@Pt NS cathode clearly displayed superior stability than Pt/C within a 65-hr testing period (Fig. 6c). When optimizing the catalyst utilization, particularly with a low anode PGM loading of 0.05 mg_{metal} cm^{-2}, we achieved an PPD of 1.30 W cm^{-2} and a total PGM loading (including anode and cathode) of 0.06 mg_{metal} cm^{-2}, which is 52% lower than the US DOE PGM target loading (Fig. 6d)[43–46]. When assessed in terms of total specific catalyst cost (normalized to the PPD), our AEMFC can cut the cost down to US$ 1.27 kW^{-1}. This value corresponds to 4% of the US DOE ultimate cost target (with PGM in both electrodes), representing an important milestone (Fig. 6d and Table S2-3).

To summarize, we have successfully bridged the knowledge gap for catalyst design for the ORR in alkaline media using a modified volcano plot. Guided by this rationale, we designed and synthesized PdH_x@Pt NS catalysts with a unique sandwich-based core-shell configuration, in which Pt nanosheets form along PdH_x NS with {111} facets and expansive strain. Comprehensive characterization, including *operando* XAS and DEMS, further validated the modified volcano plot for catalyst design, and established that the dominant {111} facet and suppressed carbon corrosion

are responsible for the improved ORR activity and stability. More importantly, AEMFCs based on PdH_x@Pt NS cathodes displayed record-high fuel cell performance with ultra-low PGM cathode loading down to 10 μg cm^{-2}. Thus, the impressive ORR performance of PdH_x@Pt NS played a key role in achieving both the US DOE loading and the ultimate cost target. This work represents a proof-of-concept for rational catalyst design, not only for AEMFC technologies, but more broadly for a variety of renewable energy applications.

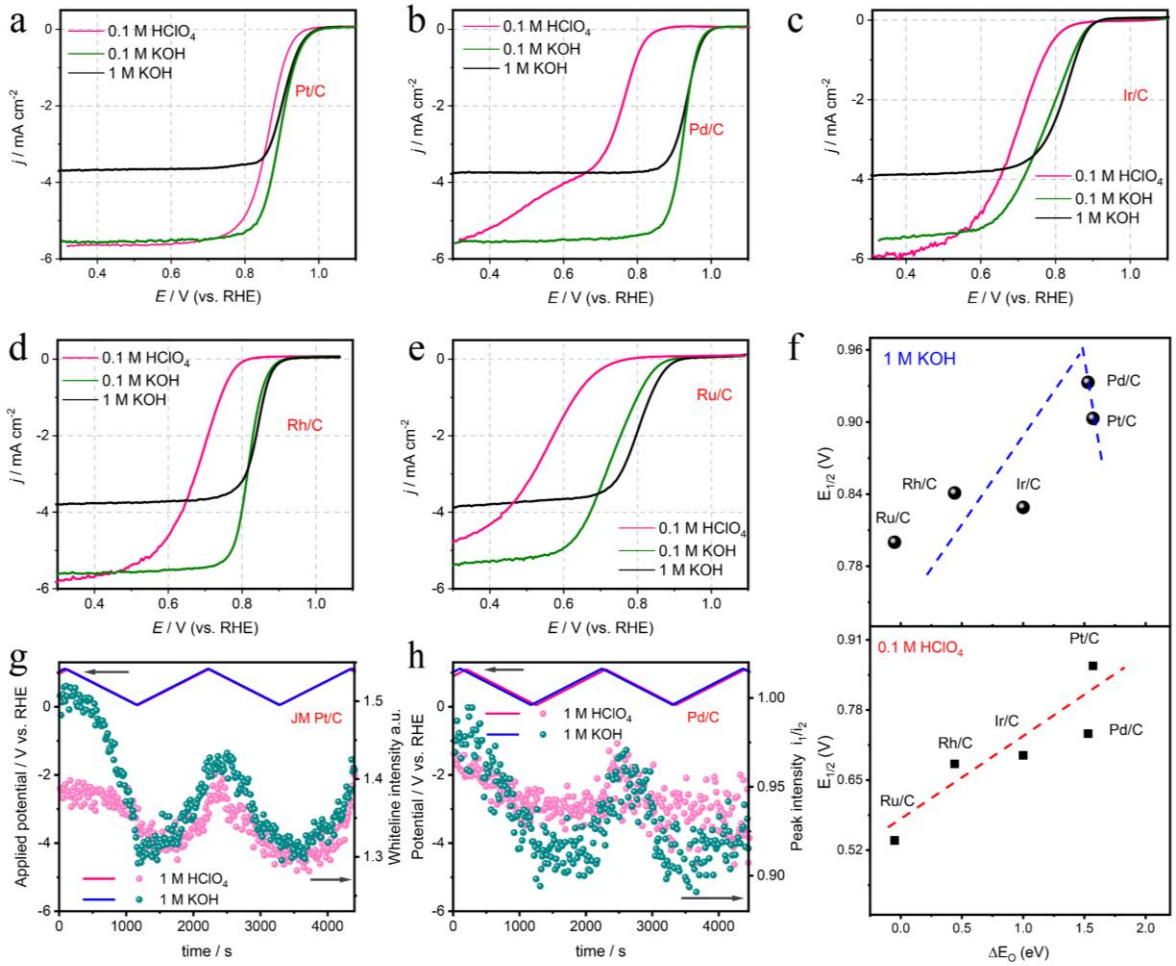

Fig. 1 Oxygen reduction reaction (ORR) on Pt/C, Pd/C, Ir/C, Rh/C and Ru/C in acidic and alkaline electrolytes. a-e, ORR polarization curves for Pt/C (**a**), Pd/C (**b**), Ir/C (**c**), Rh/C (**d**) and Ru/C (**e**), evaluated by RDE in O_2-saturated 0.1 M $HClO_4$, 0.1 M KOH and 1.0 M KOH solutions. Scan rate: 5 mV/s; rotation rate: 1,600 rpm. To effectively compare the activities of these catalysts with half wave potentials, the catalysts loadings were varied from 15 to ~20 μg cm^{-2} to attain similar electrochemical surface area. **f**, Trend of ORR half wave potentials in 1.0 M KOH and 0.1 M $HClO_4$ plotted as a function of the oxygen binding energy, ΔE_O. The ΔE_O data were acquired from the literature[7]. **g**, White line intensity of XANES spectra at the Pt L_3-edge of Pt/C as a function of time, with the applied potentials cycling between 0.05 V and 1.1 V. Since the white line intensity arises from a transition from 2p to 5d orbitals, the intensity provides information on the occupation of the 5d orbitals. Thus, a stronger white line indicates a higher oxidation state of Pt. **h**, The intensity ratio of peak-1 (i_1) and peak-2 (i_2) of XANES spectra at Pd K-edge of Pd/C as a function of time, with the applied potentials cycling between 0.05 V and 1.1 V. The definition and identity of peak-1 and peak-2 can be found in Fig.S4. Generally, a relatively larger i_1/i_2 value indicates a higher oxidation state of Pd. The measurements were conducted in O_2-saturated 1.0 M $HClO_4$ (red) and 1.0 M KOH (blue).

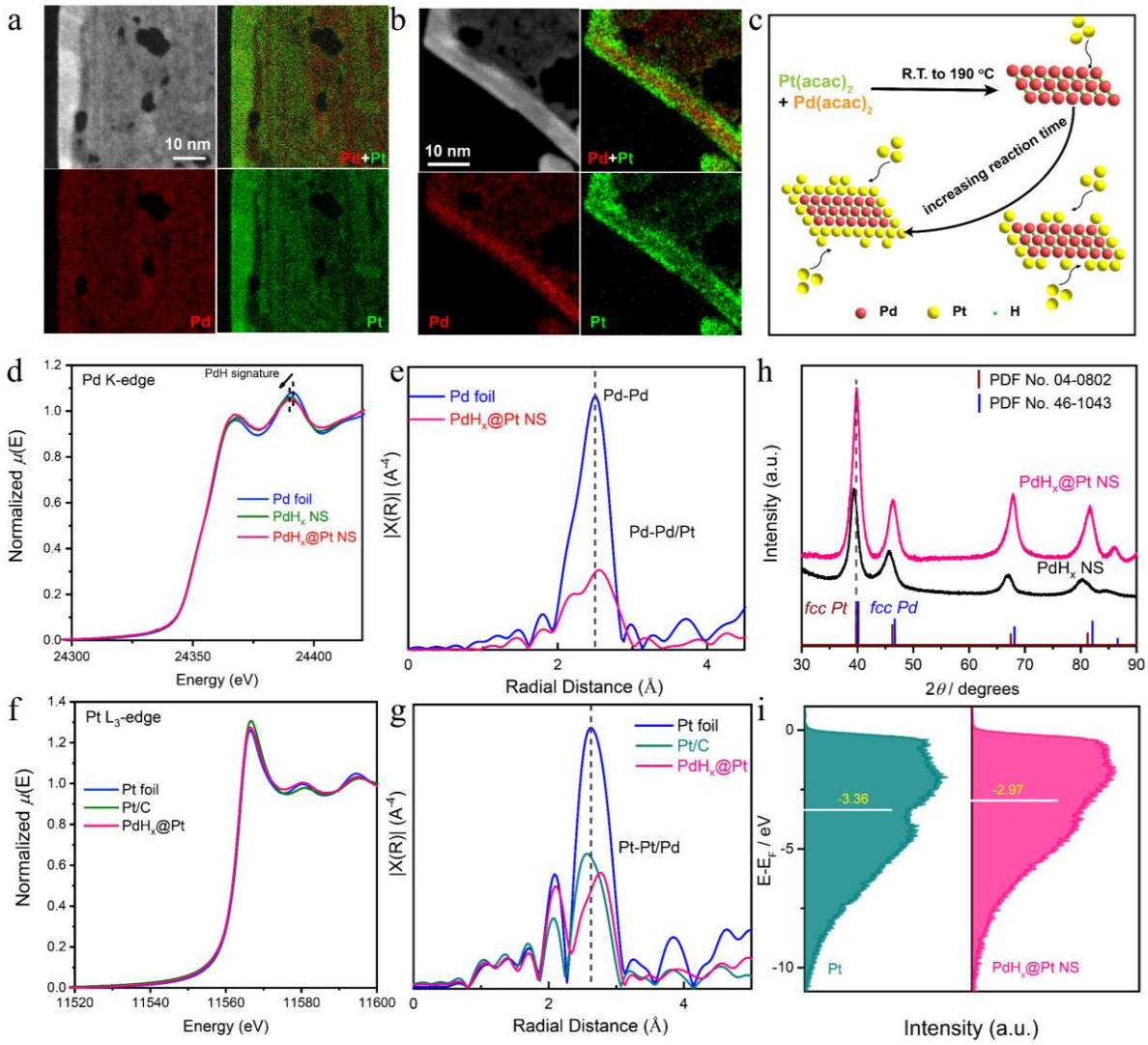

Fig. 2 Structural characterizations of PdH_x@Pt NS catalyst: a-b, HAADF-STEM image, and EDX elemental mapping of PdH_x@Pt NS. This clearly shows a sandwich-like core-shell structure with Pd forming the core and Pt forming the shell. **c**, Schematic illustration depicting the time evolution of PdH_x@Pt NS formation during synthesis. **d-e**, XANES spectra and Fourier transform (FT) of k^3-weighted EXAFS spectra at Pd K-edge of PdH_x@Pt NS. PdH_x NS and Pd foil are used as references. **f-g**, XANES spectra and Fourier transform (FT) of k^3-weighted EXAFS spectra at Pt L_3-edge of PdH_x@Pt NS. Pt/C and Pt foil are used as references. **h**, XRD patterns of PdH_x@Pt NS and PdH_x NS. **i**, XPS valence band spectra of PdH_x@Pt NS and Pt/C. All these spectra were background corrected. The white bar labeled in the spectra indicates the *d*-band center of gravity of the metal catalyst[47]. Compared to Pt, PdH_x@Pt NS displayed an upshift of the d-band center, corresponding to a stronger binding strength of reaction intermediates in the ORR[33,48].

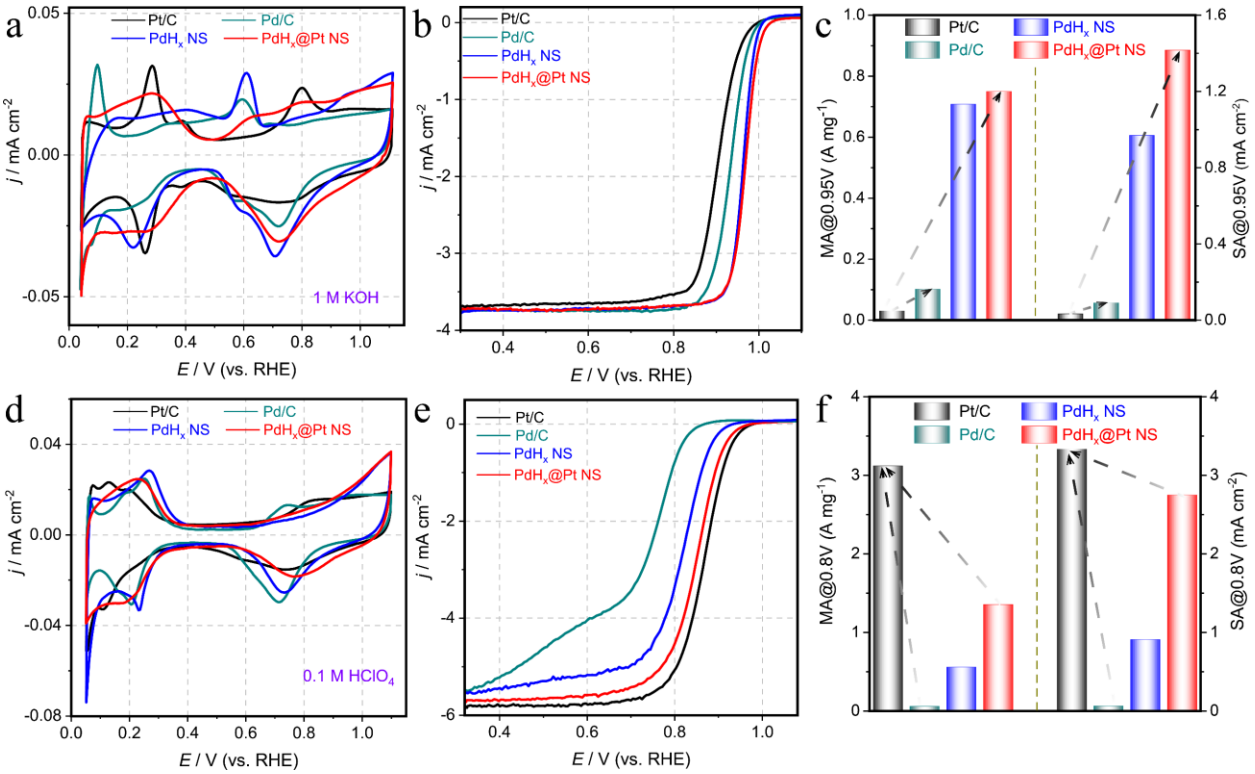

Fig. 3 Electrochemical properties of PdH$_x$@Pt NS catalyst. **a-c**, Electrochemical evaluation of PdH$_x$@Pt NS, PdH$_x$ NS, Pt/C and Pd/C in 1.0 M KOH. Cyclic voltammograms (CVs) in Ar-saturated electrolyte (**a,** 20 wt.%; loading: 15 μg/cm^2; scan rate: 20 mV/s), ORR polarization curves in O_2-saturated electrolyte (**b,** 20 wt.%; loading: 15 μg/cm^2; scan rate: 5 mV/s; rotation rate: 1,600 rpm) and corresponding mass and specific activities calculated at 0.95 V vs. RHE (**c**). **d-f**, Electrochemical evaluation of PdH$_x$@Pt NS, PdH$_x$ NS, Pt/C and Pd/C in 0.1 M $HClO_4$. CVs in Ar-saturated electrolyte (**d**), ORR polarizations in O_2-saturated electrolyte (**e**) and corresponding mass and specific activities calculated at 0.80 V vs. RHE (**f**).

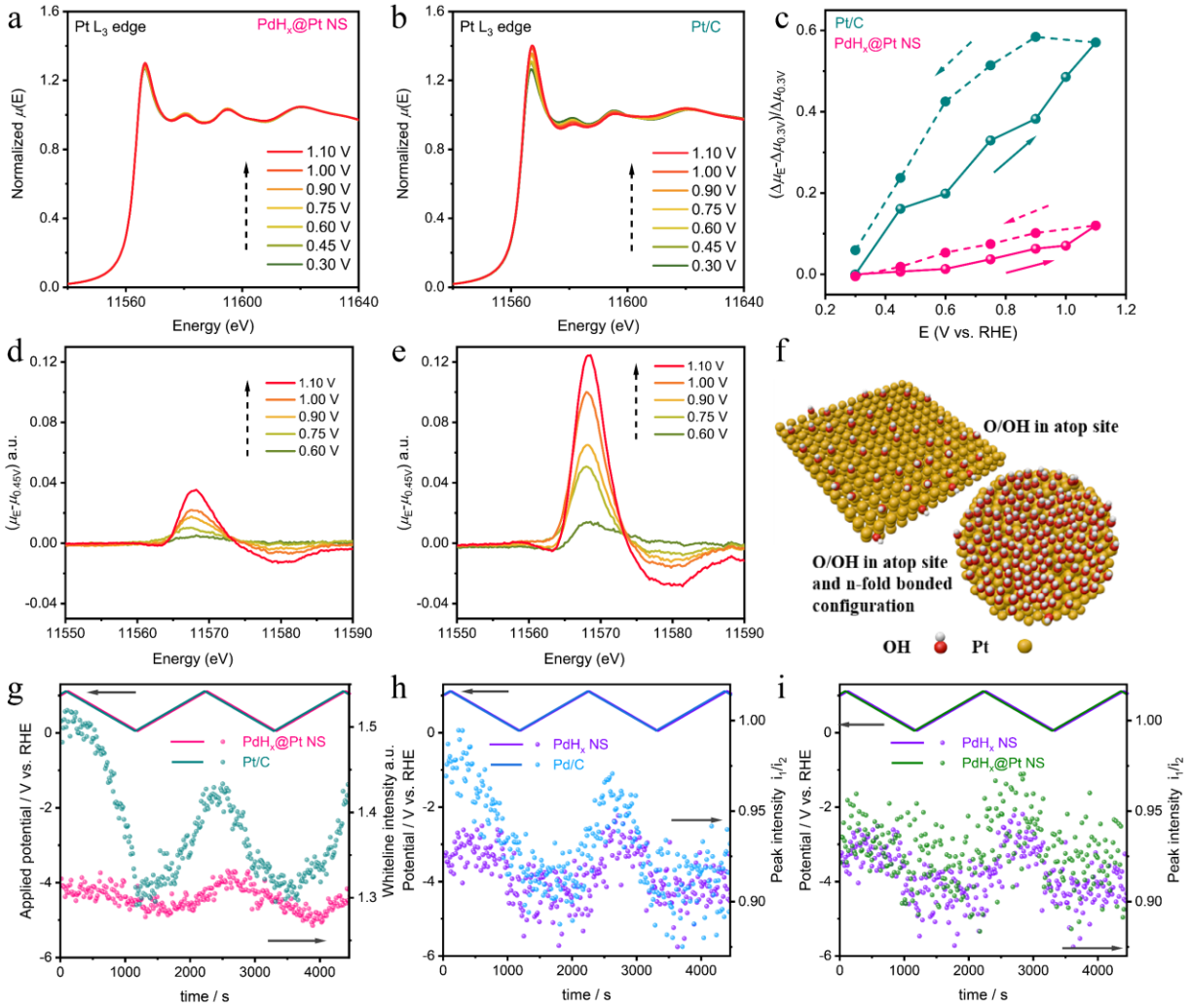

Fig. 4 *Operando* XAS studies of PdH_x@Pt NS and Pt/C under electrochemical conditions. a-b, *Operando* XANES spectra at Pt L_3-edge of PdH_x@Pt NS (**a**) and Pt/C (**b**) under steady-state conditions with potentials increasing from 0.3 V to 1.1 V (vs. RHE) in 1.0 M KOH solution. Corresponding spectra with potentials decreasing from 1.1 V to 0.3 V are shown in SI (Fig. S11). **c**, Relative changes in absorption peaks ($(\Delta\mu_E-\Delta\mu_{0.3V})/\Delta\mu_{0.3V}$, see Fig. S12 for details) at Pt L_3-edge of PdH_x@Pt NS and Pt/C plotted as a function of applied potentials. **d-e**, Pt L_3-edge $\Delta\mu$(E) spectra of PdH_x@Pt NS (**d**) and Pt/C (**e**), acquired using the expression $\Delta\mu(E)=\mu(E)-\mu(0.45\ V)$. This analysis involves subtracting a reference spectrum (assuming no adsorbates) from the ones at different potentials and comparing them with theoretical $\Delta\mu$ curves based on crystallographic models. The $\Delta\mu$ method effectively isolates surface/adsorbate interactions while minimizing the fluence of bulk metal-metal interactions, providing valuable insights into the nature of the absorbates, their coverage and specific adsorption sites on the surface[20,38]. **f**, Schematic of OH or O adsorption on Pt nanosheet with {111} facet and Pt nanoparticle in 1.0 M KOH. **g**, The white line intensity of XANES spectra at Pt L_3-edge of Pt/C (cyan) and PdH_x@Pt NS (pink) as a function of time, with the applied potentials cycling between 0.05 V and 1.1 V in O_2-saturated 1.0 M KOH. **h-i**, The intensity ratio of peak-1 (i_1) and peak-2 (i_2) of XANES spectra at Pd K-edge of Pd/C (blue) and PdH_x NS (purple) (**h**) and PdH_x@Pt NS (green) (**i**) as a function of time, with the applied potentials cycling between 0.05 V and 1.1 V in O_2-saturated 1.0 M KOH.

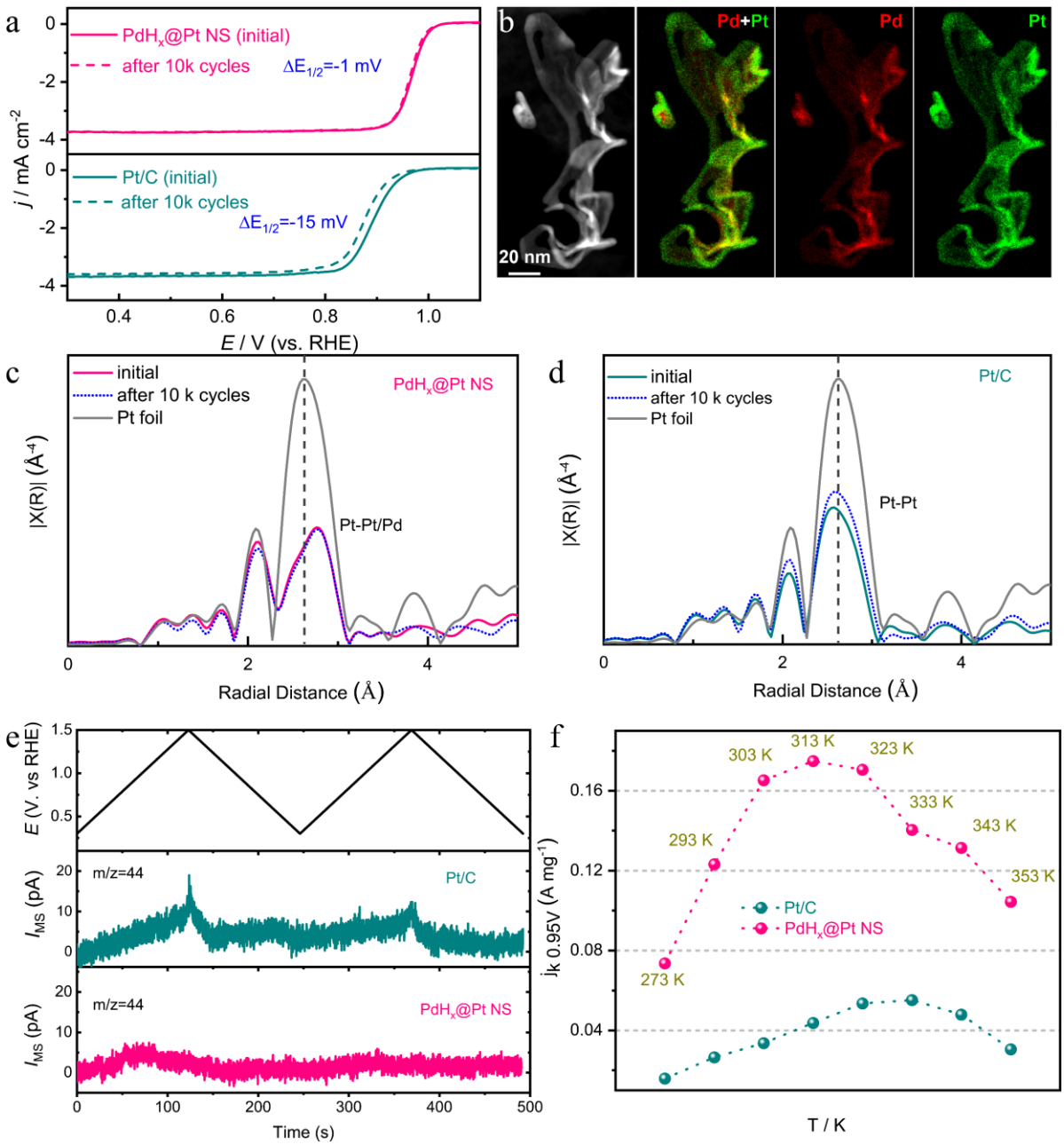

Fig. 5 ORR **performance of PdH_x@Pt NS under different conditions**. **a**, ORR polarization curves of PdH_x@Pt NS and Pt/C before and after 10,000 ADT cycles. Scan rate is 5 mV/s. **b**, HAADF-STEM image and EDX elemental mapping of PdH_x@Pt NS after 10,000 ADT cycles. **c-d**, Fourier transfer (FT) of k^3-weighted EXAFS spectra of PdH_x@Pt NS (**c**) and Pt/C (**d**) after 10,000 ADT cycles, respectively. **e**, DEMS analysis of possible CO_2 (m/z = 44) evolved due to the oxidation of carbon support in Pt/C and PdH_x@Pt NS in 0.1 M KOH solution. The potential was cycled between 0.30 V and 1.50 V at a scan rate of 10 mV/s. **f**, Temperature-dependent ORR performance of 60 wt.% Pt/C and PdH_x@Pt NS, evaluated by mass activity determined at 0.95 V in anodic scans. The activity was normalized to its corresponding O_2 concentration to eliminate the effects from the temperature-dependent solubility of oxygen.

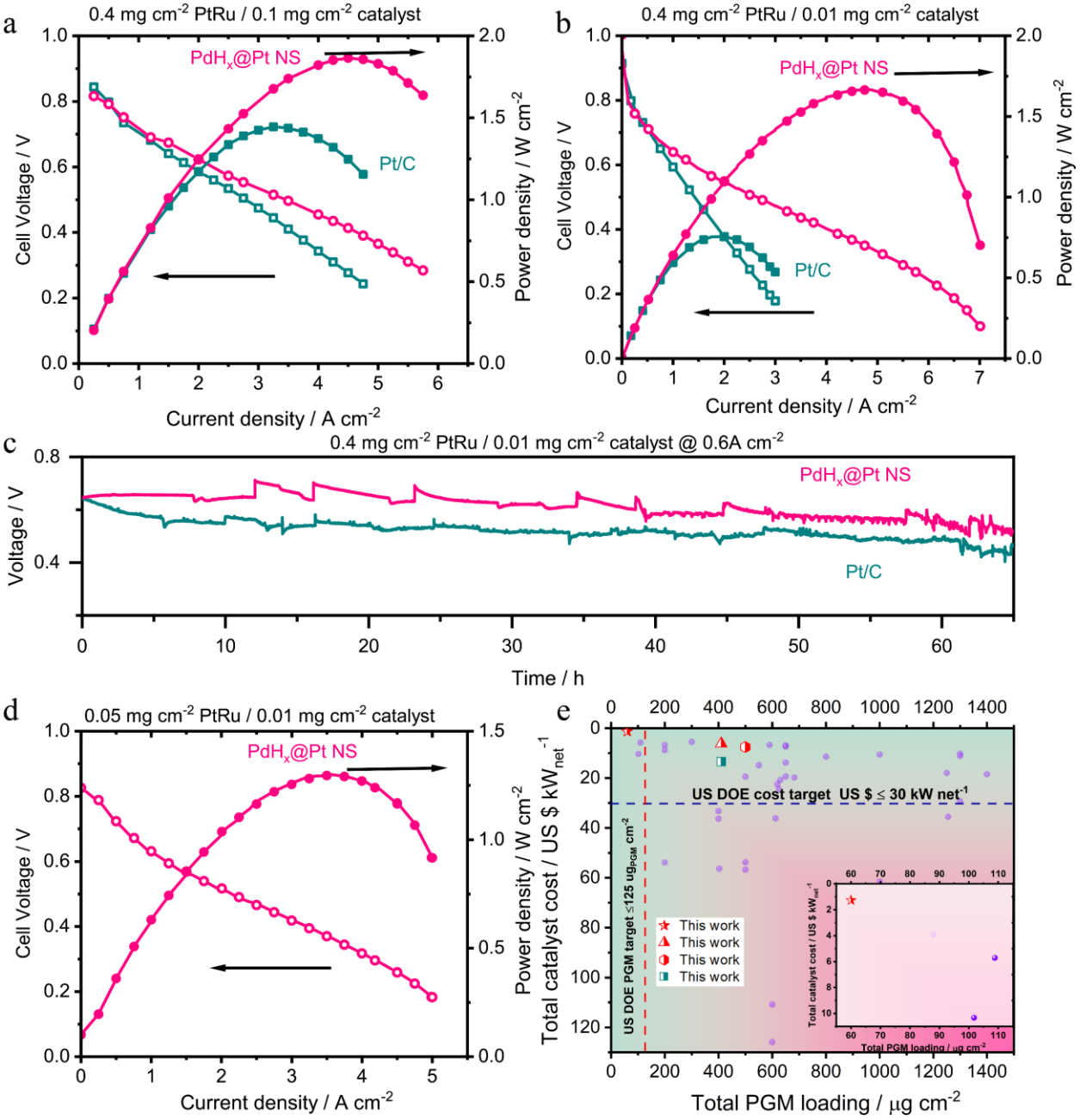

Fig. 6 AEMFC performance with PdH_x@Pt NS cathodes. **a-b**, Cell voltage and power density as a function of current densities of a single AEMFC with 60 wt.% Pt/C or PdH_x@Pt NS as the cathode and 60 wt.% PtRu as the anode (0.4 mg_{metal} cm^{-2}). Quaternary ammonium poly(N-methyl-piperidine-co-p-terphenyl) (QAPPT) was used as the anion exchange membrane. The metal loading of the cathode was controlled to 0.1 mg_{metal} cm^{-2} (**a**) and 0.01 mg_{metal} cm^{-2} (**b**), respectively. The cell was operated at 80°C and fed with fully humidified H_2 (500 sccm) and O_2 (500 sccm) with 0.2 MPa backpressure on both sides of the cell. **c**, Representative 65 hr stability tests of AEMFCs with 0.01 mg_{metal} cm^{-2} Pt/C and PdH_x@Pt NS cathodes, measured at a constant current density load of 600 mA cm^{-2}. **d**, Single AEMFC performance with reduced PGM loadings. The metal loadings were controlled to 0.01 mg_{metal} cm^{-2} for PdH_x@Pt NS cathode and 0.05 mg_{metal} cm^{-}

^{2} for PtRu/C anode. **e**, An overall analysis of total PGM loading and catalyst cost, compared to representative state-of-art PGM-based AEMFCs summarized in Supplementary Table S2-3. The x and y axis represent geometric area normalized total PGM loading and peak-power density normalized total catalyst cost, respectively. The AEMFCs studied in this work are shown as the half-filled red star, triangle and hexagon in the plot. The purple balls mark the performance metrics of representative state-of-art PGM-based AEMFCs in literature. The red dashed line indicates the US DOE loading target (<=125 μg_{PGM} cm^{-2}), while the blue dashed line denotes the US DOE ultimate cost target (<=\$30 kW_{net}^{-1}). The inset shows a zoomed-in region of AEMFCs that meets both the loading and cost targets.

Methods

Chemicals and materials. Palladium (II) acetylacetonate ($Pd(acac)_2$, 99%), Platinum (II) acetylacetonate ($Pt(acac)_2$, 97%), oleylamine (oAm, $C_{18}H_{37}N$, 70%), dimethyl sulfoxide (DMSO, ⩾99%), propyl alcohol (1-PrOH, 99.5%), ascorbic acid (AA) and potassium hydroxide (KOH, ⩾99.99%) were purchased from Sigma-Aldrich. Absolute ethanol (C_2H_5OH, 99.5%) was purchased from Fisher Scientific. High surface area Ketjen Black carbon powder (EC-300JD) was purchased from AkzoNobel. Carbon supported Pt (Pt/C, 20 and 60 wt.%), Pd (Pd/C, 20 wt.%), Rh (Rh/C, 20 wt.%), Ru (Ru/C, 20 wt.%) and PtRu catalysts (PtRu/C, 60 wt.%) were purchased from the FuelCellStore. D2021 Nafion dispersion (20 wt.%) and AvCarb MGL190 carbon paper were also purchased from the FuelCellStore. The quaternary ammonium poly(N-methylpiperidine-co-p-terphenyl) (QAPPT, IEC = 2.50±0.05 mmol/g, 25±2 μm thick) membrane and ionomer binder were obtained from Eve Energy. Deionized water (18.2 MΩ.cm) was acquired from a Barnstead Nanopure water purification system. Ultra-high purity nitrogen (UHP N_2, 99.999%), ultra-high purity Argon (UHP Ar, 99.999%), ultra-high purity hydrogen (UHP H_2, 99.999%), ultra-high purity oxygen (UHP O_2, 99.999%), and carbon monoxide (CO, 99.99%) were supplied by Airgas. All chemicals were used as received without further purification.

Preparation of PdH_x NS and PdH_x@Pt NS catalysts. In a typical synthesis procedure, 0.05 mmol of $Pd(acac)_2$ and $Pt(acac)_2$ (Pt molar ratios: 0% or 50%) were dissolved in a 20 mL vial with 6 mL of oAm at 120 °C for 5 min until the solution became clear. After the solution was cooled down, EC-300JD carbon powder and 35 mg AA were added, followed by one-hour sonication until a homogenously dispersed solution was obtained. The solution was then transferred to a 50 mL autoclave with a magnetic stirrer bar, sealed and purged with 0.3 MPa CO. The autoclave was then placed in an oil bath at 190 ºC for 3 hr under magnetic stirring (900 rpm). After the autoclave was cooled down and vented, the catalysts were collected using a centrifuge at 8,000 rpm for 3 min. The precipitates were then washed five times with EtOH and hexane (vol. 1:1) and dried at 60 ºC for 2 hr.

Preparation of carbon supported Ir (Ir/C, 20 wt.%). Ir/C was prepared following our previous work[49]. In brief, 15.5 mg $IrCl_3 \cdot xH_2O$ and 40 mg EC-300JD carbon powder were dispersed in 10 mL water in a beaker with 30-min sonication. The solution was then heated with magnetic stirring on a hot plate to form a slurry. The slurry was then sonicated for 10 min and then dried at 60 ºC in an oven for 10 hr. The dried sample was ground into a powder and annealed in a flow furnace under a forming gas (5% H_2/N_2) atmosphere at 400 ºC for 2 hr.

Physicochemical characterization. Powder X-ray diffraction (XRD) patterns were collected on a Rigaku Ultima IV Diffractometer (Cu Kα λ=1.5406 Å) operated at 1.76 kW (40 kV and 44 mA). EDX mappings

and HADDF-STEM images were conducted conducted with Thermo Scientific Spectra 300 Ultra S/TEM (120 kV) and FEI Tecnai F20 TEM/STEM (200 kV). The 4D-STEM data were collected using Thermo-Fisher Titan Themis Cryo S/TEM with a Field Emission Gun (X-FEG) and a monochromator, operated at 300 kV and room temperature. The dataset was acquired with C2 aperture of 10 um, camera length of 1.5 m, and convergence angle of 0.12 mrad in microprobe mode, utilizing Electron Microscope Pixel Array Detector (EMPAD) GII. The settings included a dwell time of 100 μs and a total dose of 800 $e^-/Å$. XPS measurements were carried out using a Scienta Omicron ESCA-2SR with monochromatic Al Kα X ray (1486.6 eV). XAS spectra of Pd K-edge and Pt L_3-edge were acquired at the beamline ISS 8-ID of the National Synchrotron Light Source II (NSLS-II), Brookhaven National Laboratory (BNL).

Electrochemical measurements. The RDE experiments were performed in a conventional three-electrode cell with a WaveDriver200 potentiostat from Pine Instruments. Before the measurements, the three-electrode cell was soaked in aqua regia and rinsed with deionized water several times to remove any contaminants. The catalyst ink solutions (5 mg/mL) were prepared by dispersing catalysts (20 wt% or 60 wt%) in 0.25 wt.% Nafion/ethanol solution, followed by sonication for around 30 min to form homogenous catalyst inks. Thin-film electrodes were made by drop casting the ink onto a glassy carbon electrode (d = 5mm) with a pipet, achieving a metal loading of 15 μg cm^{-2} (loading for Fig. 2). The loadings shown in Fig. 1 were adjusted from 15 to ~20 μg cm^{-2} to accommodate the difference in electrochemical surface area, since the half-wave potentials in ORR polarization curves were used to compare the activities of PGM-group metal particles supported on carbon. A high-surface area graphite rod (99.995%) was used as the counter electrode and a Ag/AgCl (saturated KCl) electrode served as the reference electrode. All potentials reported in this work are referenced to the RHE, which was calibrated in the same electrolyte using the potential at zero current of the hydrogen oxidation/evolution reaction (HOR/HER) polarization curves on a polycrystalline Pt electrode. Cyclic voltammograms for all the samples were performed in UHP Ar saturated electrolyte solutions from 0.05-1.1 V vs. RHE at a scan rate of 20 mV s^{-1}. The ORR polarization curves were acquired in UHP O_2 saturated electrolyte from 0.30-1.10 V vs. RHE at a sweep rate of 5 mV s^{-1} and a rotation rate of 1,600 rpm. The electrochemical surface areas (ECSA) of all the catalysts were determined by CO stripping experiment.

XAS measurement and analysis. All the *operando* XAS spectra of Pd K-edge and Pt L_3-edge were collected in fluorescence mode under real-time electrochemical conditions using a home-made electrochemical cell set-up at room temperature, at the beamline ISS 8-ID of the NSLS-II. Details of design and operation of the home-made electrochemical cell can be found in our previous study[50]. The preparation of the catalyst electrode for *operando* XAS experiments was similar to the RDE except that the ink was drop-cast onto a one end (1×1 cm^2) of a piece of carbon paper (1×6 cm^2, AvCarb MGL190, Fuel Cell Store),

which worked as both non-active and support with negligible effects on the catalytic current. The loading of the catalyst was 0.1 mg/cm^2. Prior to XAS measurement, the electrode surface was cleaned by several potential cycles. The *operando* XAS spectra data were collected at potentiodynamic (non-steady) or potentiostatic (steady-state) modes. For the potentiodynamic mode, the XANES spectra of Pd K-edge or Pt L_3-edge were recorded under potential scan from 0.05 V to 1.10 V vs RHE with a scan rate of 1 mV/s. The spectra were collected every 15 seconds, including 10 seconds for tuning monochromators and 5 seconds for data acquisition), giving rise to a potential resolution of 15 mV. For the steady-state mode, the XAS spectra including both XANES and EXAFS were collected with varied applied potentials increasing from 0.30 V to 1.10 V and decreasing from 1.10 V to 0.30 V. All the XAS data were analyzed with the Athena software packages[51].

DEMS study for carbon corrosion. The DEMS measurement for CO_2 monitoring was performed at room temperature with a custom-built cell. A detailed description of the DEMS setup can be found in our previous work[42]. The working electrode was prepared by drop-casting 10 µL catalyst ink onto a piece of gold sputtered (~100 nm) porous PTFE membrane and followed by drying with an infrared lamp. The working electrode was then assembled between a stainless-steel frit and PTFE gasket. A Pt coil served as the counter electrode and a Ag/AgCl (saturated KCl) electrode was used as the reference electrode. During the experiment, CO_2 evolved from the working electrode (with catalyst) can easily access the vacuum chamber through the porous membrane, rather than undergoing carbonation with hydroxide species in the solution. Thus, the generated CO_2 can be detected by a quadrupole mass spectrometer in less than 1 s. Before executing the experiment, ~4 mL 0.1 M KOH solution was transferred to the electrochemical cell and purged with oxygen for at least 20 min to remove any residual air from the solution. Controlled potential scans were applied to the system with a potentiostat from Pine Instrument while a home-made LabVIEW program was used to record the mass spectrometric signals at m/z = 44, corresponding to CO_2^+. The collected data for CO_2 were processed by subtracting the background signals.

AEMFC assembly and testing. The alkaline polymer membrane and ionomer binder used in the MEA were QAPPT[52]. In brief, the catalyst/ionomer binder with a mass ratio of 4:1 was dispersed in a mixture of n-propanol and ethanol under sonication, and then spray-coated onto the two sides of the QAPPT membrane with a geometric area of 4 cm^2 on a heated vacuum table at 72 °C. The catalyst loadings in the cathode or anode were varied to optimize the MEA performance. The as-prepared CCM was then soaked in 1.0 M KOH at 60 ºC for 10 hr to exchange Cl^- with OH^- and rinsed with deionized water for several times prior to assembly. The resulting CCM was placed between two pieces of Teflon-treated carbon paper (AvCarb MGL190) and assembled with bipolar plates and Teflon gaskets, tightened with 6 N·m torque. Single AEMFC performance was evaluated at 80 ºC in an 850e fuel cell test system from Scribner Associates.

Fully humidified O_2 and H_2 gases were supplied to the cell with a gas back pressure of 0.2 MPa on both sides.

Data availability

The data supporting the findings of this study are available in the paper and its Supplementary Information. Extra data are available from the corresponding authors on reasonable request.

References

1. Britton, B. *et al.* Perspective—the next decade of AEMFCs: near-term targets to accelerate applied R&D. *J. Electrochem. Soc.* **167**, 084514 (2020).
2. Luo, M. & Koper, M. T. M. A kinetic descriptor for the electrolyte effect on the oxygen reduction kinetics on Pt(111). *Nat. Catal.* **5**, 615–623 (2022).
3. She, Z. W. *et al.* Combining theory and experiment in electrocatalysis: Insights into materials design. *Science* **355**, eaad4998 (2017).
4. Ooka, H., Huang, J. & Exner, K. S. The Sabatier Principle in Electrocatalysis: Basics, Limitations, and Extensions. *Front. Energy Res.* **9**, 654460 (2021).
5. Sabatier, P. How I Have Been Led to the Direct Hydrogenation Method by Metallic Catalysts. *Ind. Eng. Chem.* **18**, 1005–1008 (1926).
6. Kulkarni, A., Siahrostami, S., Patel, A. & Nørskov, J. K. Understanding Catalytic Activity Trends in the Oxygen Reduction Reaction. *Chem. Rev.* **118**, 2302–2312 (2018).
7. Nørskov, J. K. *et al.* Origin of the overpotential for oxygen reduction at a fuel-cell cathode. *J. Phys. Chem. B* **108**, 17886–17892 (2004).
8. Wang, Y. J. *et al.* Carbon-Supported Pt-Based Alloy Electrocatalysts for the Oxygen Reduction Reaction in Polymer Electrolyte Membrane Fuel Cells: Particle Size, Shape, and Composition Manipulation and Their Impact to Activity. *Chem. Rev.* **115**, 3433–3467 (2015).
9. Lim, C., Fairhurst, A. R., Ransom, B. J., Haering, D. & Stamenkovic, V. R. Role of Transition Metals in Pt Alloy Catalysts for the Oxygen Reduction Reaction. *ACS Catal.* **13**, 14874–14893 (2023).
10. Stamenkovic, V. R., Strmcnik, D., Lopes, P. P. & Markovic, N. M. Energy and fuels from electrochemical interfaces. *Nat. Mater.* **16**, 57–69 (2016).
11. Li, H. *et al.* Oxidative Stability Matters: A Case Study of Pallidum Hydride Nanosheets for Alkaline Fuel Cells. *J. Am. Chem. Soc.* **2022**, 8114 (2022).
12. Zhou, M. *et al.* Improvement of Oxygen Reduction Performance in Alkaline Media by Tuning Phase Structure of Pd-Bi Nanocatalysts. *J. Am. Chem. Soc.* **143**, 15891–15897 (2021).
13. Wang, L. *et al.* Tunable intrinsic strain in two-dimensional transition metal electrocatalysts. *Science*

363, 870–874 (2019).

14. Luo, M. *et al.* PdMo bimetallene for oxygen reduction catalysis. *Nature* **574**, 81–85 (2019).
15. Gómez-Marín, A. M., Rizo, R. & Feliu, J. M. Oxygen reduction reaction at Pt single crystals: a critical overview. *Catal. Sci. Technol.* **4**, 1685–1698 (2014).
16. Li, M. F., Liao, L. W., Yuan, D. F., Mei, D. & Chen, Y. X. pH effect on oxygen reduction reaction at Pt(1 1 1) electrode. *Electrochim. Acta* **110**, 780–789 (2013).
17. Friebel, D. *et al.* In situ X-ray probing reveals fingerprints of surface platinum oxide. *Phys. Chem. Chem. Phys.* **13**, 262–266 (2010).
18. McCaulley, J. A. In-situ X-ray absorption spectroscopy studies of hydride and carbide formation in supported palladium catalysts. *J. Phys. Chem.* **97**, 10372–10379 (1993).
19. Liu, G. *et al.* Hydrogen-Intercalation-Induced Lattice Expansion of Pd@Pt Core-Shell Nanoparticles for Highly Efficient Electrocatalytic Alcohol Oxidation. *J. Am. Chem. Soc.* **143**, 11262–11270 (2021).
20. Sasaki, K., Marinkovic, N., Isaacs, H. S. & Adzic, R. R. Synchrotron-Based in Situ Characterization of Carbon-Supported Platinum and Platinum Monolayer Electrocatalysts. *ACS Catal.* **6**, 69–76 (2016).
21. Takimoto, D. *et al.* Platinum nanosheets synthesized via topotactic reduction of single-layer platinum oxide nanosheets for electrocatalysis. *Nat. Commun.* **14**, 19 (2023).
22. Stamenkovic, V. R. *et al.* Improved oxygen reduction activity on $Pt_3Ni(111)$ via increased surface site availability. *Science* **315**, 493–497 (2007).
23. Liang, Y., McLaughlin, D., Csoklich, C., Schneider, O. & Bandarenka, A. S. The nature of active centers catalyzing oxygen electro-reduction at platinum surfaces in alkaline media. *Energy Environ. Sci.* **12**, 351–357 (2019).
24. Govindarajan, N., Xu, A. & Chan, K. How pH affects electrochemical processes. *Science* **375**, 379–380 (2022).
25. Kelly, S. R., Kirk, C., Chan, K. & Nørskov, J. K. Electric field effects in oxygen reduction kinetics: rationalizing pH dependence at the Pt(111), Au(111), and Au(100) electrodes. *J. Phys. Chem. C* **124**, 14581–14591 (2020).
26. Briega-Martos, V., Herrero, E. & Feliu, J. M. Effect of pH and Water Structure on the Oxygen Reduction Reaction on platinum electrodes. *Electrochim. Acta* **241**, 497–509 (2017).
27. Li, H. *et al.* Analysis of the limitations in the oxygen reduction activity of transition metal oxide surfaces. *Nat. Catal.* **4**, 463–468 (2021).
28. Tian, X. *et al.* Engineering bunched Pt-Ni alloy nanocages for efficient oxygen reduction in practical fuel cells. *Science* **366**, 850–856 (2019).

29. Wang, Q. *et al*. Unveiling the Pitfalls of Comparing Oxygen Reduction Reaction Kinetic Data for Pd-Based Electrocatalysts without the Experimental Conditions of the Current−Potential Curves. *ACS Energy Lett.* **7**, 952–957 (2022).
30. He, T. *et al.* Mastering the surface strain of platinum catalysts for efficient electrocatalysis. *Nature* **598**, 76–81 (2021).
31. Bugaev, A. L. *et al.* Palladium Carbide and Hydride Formation in the Bulk and at the Surface of Palladium Nanoparticles. *J. Phys. Chem. C* **122**, 12029–12037 (2018).
32. Kabiraz, M. K. *et al.* Ligand Effect of Shape-Controlled β-Palladium Hydride Nanocrystals on Liquid-Fuel Oxidation Reactions. *Chem. Mater.* **31**, 5663–5673 (2019).
33. Zhang, J. *et al.* Controlling the Catalytic Activity of Platinum-Monolayer Electrocatalysts for Oxygen Reduction with Different Substrates. *Angew. Chem. Int. Ed.* **44**, 2132–2135 (2005).
34. Xu, Y., Ruban, A. V & Mavrikakis, M. Adsorption and Dissociation of O_2 on Pt-Co and Pt-Fe Alloys. *J. Am. Chem. Soc.* **126**, 4717-4725 (2004).
35. Rizo, R., Sitta, E., Herrero, E., Climent, V. & Feliu, J. M. Towards the understanding of the interfacial pH scale at Pt(1 1 1) electrodes. *Electrochim. Acta* **162**, 138–145 (2015).
36. Kuo, D. Y., Lu, X., Hu, B., Abruña, H. D. & Suntivich, J. Rate and Mechanism of Electrochemical Formation of Surface-Bound Hydrogen on Pt(111) Single Crystals. *J. Phys. Chem. Lett.* **13**, 6383–6390 (2022).
37. Editor, G. *et al.* Stripping voltammetry of carbon monoxide oxidation on stepped platinum single-crystal electrodes in alkaline solution. *Phys. Chem. Chem. Phys.* **10**, 3802–3811 (2008).
38. Jia, Q. *et al.* Activity descriptor identification for oxygen reduction on platinum-based bimetallic nanoparticles: In situ observation of the linear composition-strain-activity relationship. *ACS Nano* **9**, 387–400 (2015).
39. Roth, C. *et al.* Determination of O[H] and CO coverage and adsorption sites on PtRu electrodes in an operating PEM fuel cell. *J. Am. Chem. Soc.* **127**, 14607–14615 (2005).
40. Teliska, M., O'Grady, W. E. & Ramaker, D. E. Determination of O and OH adsorption sites and coverage in situ on Pt electrodes from Pt L_{23} X-ray absorption spectroscopy. *J. Phys. Chem. B* **109**, 8076–8084 (2005).
41. Meier, J. C. *et al.* Design criteria for stable Pt/C fuel cell catalysts. *Beilstein J. Nanotechnol.* **5**, 44–67 (2014).
42. Zeng, R. *et al.* Methanol Oxidation Using Ternary Ordered Intermetallic Electrocatalysts: A DEMS Study. *ACS Catal.* **10**, 770–776 (2020).
43. Wang, X. X., Swihart, M. T. & Wu, G. Achievements, challenges and perspectives on cathode catalysts in proton exchange membrane fuel cells for transportation. *Nat. Catal.* **2**, 578–589 (2019).

44. Hydrogen and Fuel Cell Technologies Office *DOE* Technical Targets for Polymer Electrolyte Membrane Fuel Cell Components (US DOE, 2022); https://www.energy.gov/eere/fuelcells/doe-technical-targets-polymer-electrolyte-membrane-fuel-cell-components.
45. Setzler, B. P., Zhuang, Z., Wittkopf, J. A. & Yan, Y. Activity targets for nanostructured platinum-group-metal-free catalysts in hydroxide exchange membrane fuel cells. *Nat. Nanotechnol.* **11**, 1020–1025 (2016).
46. Douglin, J. C. *et al.* High-performance ionomerless cathode anion-exchange membrane fuel cells with ultra-low-loading Ag–Pd alloy electrocatalysts. *Nat. Energy* **8**, 1262–1272 (2023).
47. Kim, D., Resasco, J., Yu, Y., Asiri, A. M. & Yang, P. Synergistic geometric and electronic effects for electrochemical reduction of carbon dioxide using gold–copper bimetallic nanoparticles. *Nat. Commun.* **5**, 4948 (2014).
48. Lima, F. H. B. *et al.* Catalytic activity - d-band center correlation for the O_2 reduction reaction on platinum in alkaline solutions. *J. Phys. Chem. C* **111**, 404–410 (2007).
49. Wang, H. & Abruña, H. D. IrPdRu/C as H_2 Oxidation Catalysts for Alkaline Fuel Cells. *J. Am. Chem. Soc.* **139**, 6807–6810 (2017).
50. Yang, Y. *et al.* In Situ X-ray Absorption Spectroscopy of a Synergistic Co-Mn Oxide Catalyst for the Oxygen Reduction Reaction. *J. Am. Chem. Soc* .**141**, 1463–1466 (2019).
51. Ravel, B. & Newville, M. ATHENA, ARTEMIS, HEPHAESTUS: data analysis for X-ray absorption spectroscopy using IFEFFIT. *J. Synchrotron Radiat.* **12**, 537–541 (2005).
52. Yang, Y. *et al.* High-Loading Composition-Tolerant Co-Mn Spinel Oxides with Performance beyond 1 W/cm^2 in Alkaline Polymer Electrolyte Fuel Cells. *ACS Energy Lett.* **4**, 1251–1257 (2019).

Acknowledgements

This work was supported by the Center for Alkaline Based Energy Solutions (CABES), part of the Energy Frontier Research Center (EFRC) program supported by the U.S. Department of Energy (DOE), Office of Science, Office of Basic Energy Sciences under Grant DE-SC-0019445. This work made use of TEM facilities at the Cornell Center for Materials Research (CCMR) which are supported through the National Science Foundation Materials Research Science and Engineering Center (NSF MRSEC) program (DMR1719875). This research used ISS (8-ID) beamline of the National Synchrotron Light Source II, a U.S. Department of Energy, Office of Science User Facility operated for the DOE Office of Science by Brookhaven National Laboratory under Contract No. DE-SC0012704.

Author contributions

H.L., R.Z. and H.D.A. conceived the research and wrote the paper. H.L., R.Z. and H.W. performed catalysts synthesis, electrochemical measurements, and general characterization. Z.S. conducted STEM/EDX characterization and analysis, supervised by D.M.. H.L., R.Z., D.L., and E.S. performed *operando* XAS characterization. H.L. and R.Z. handled XAS data analysis and *operando* XAS electrochemical cell design with the help of M.M.T-C., W.X. and A.M.V.. H.L. did MEA testing with the assistance of Q.L., A.M.V. and M.K.. H.D.A. supervised the research. All the authors contributed to the discussions and revisions of the manuscript.

Competing interests

The authors declare no competing interests.